Phase-field crystal model for materials with anomalous expansion during solidification and its application to the cavitation of supercooled water droplets

Paul Jreidini and Nikolas Provatas
Department of Physics and Centre for the Physics of Materials, McGill University, Montreal, Canada H3A 2T8

(Received 8 March 2022; revised 13 May 2022; accepted 18 May 2022; published 31 May 2022)

Unlike most pure materials, liquid water and silicon exhibit a decrease in density upon solidification, a behavior with important implications for natural and industrial processes. In this work, we propose a modification to previous vapor-liquid-solid phase-field crystal (PFC) models that allows the simulation of such anomalous density changes upon solidification. We describe the differences between the original and modified PFC models' phase diagrams and energy landscapes, specifically highlighting the equilibrium properties of the anomalous density model. The model is used to simulate a deeply quenched liquid droplet undergoing solidification under the assumption of two-time dynamics to allow for rapid elastic relaxation. Overpressurization-induced cavitation and damped oscillator behavior are observed within the simulated droplet, in agreement with recent experiments on supercooled water droplets.

DOI: 10.1103/PhysRevMaterials.6.053404

I. INTRODUCTION

The majority of crystalline materials undergo a density increase during a transition from a liquid to solid state. However, the few materials that exhibit the opposite behavior include hexagonal ice—the most common form of solid water on Earth—as well as crystalline silicon, ubiquitous in modern electronics. This anomalous density change has important implications for both natural and industrial processes. For example, the expansion of ice plays a role in freeze-induced damage to porous construction and geological materials [1–3], affects meteorological phenomena due to the explosive fragmentation of supercooled microscopic water droplets in the upper atmosphere [4,5], and imposes challenges to technological innovations ranging from hydrogen fuel cells [6] to spacecraft thermal control systems [7]. As for silicon, the anomalous expansion modifies the electronic band structure in silicon microspheres due to compressive stresses [8], provides the shear stresses that drive dislocation generation during directional solidification [9,10], and otherwise affects the microstructure in additively manufactured samples [11] and laser-melted thin films [12].

The wide variety of phenomena tied to anomalous expansion during solidification, coupled with the range of length and time scales involved, complicates the choice of modeling technique one would use in their study. Molecular dynamics (MD) is useful in examining the very early stages of ice nucleation where the complex behavior of hydrogen bonds dominates [13], and can in general simulate the crystalline structures typical in materials that undergo anomalous expansion including silicon and hexagonal ice [14]. However, MD is typically constrained to nanosecond timescales, limiting the solidification speeds and sizes possible to study. On the opposite end of the scale, phase-field (PF) models are widely used for mesoscale solidification simulation [15], including for silicon [16], but have difficulty in naturally accounting for crucial microscopic information such as lattice orientation, deformation, and defects. In this work, we choose to focus on phase-field crystal (PFC) methodology, an offshoot of traditional PF models that retains crystalline structure information typically seen in atomic-resolution models, while concomitantly allowing the simulation of solidification at diffusive timescales [17,18]. We additionally take advantage of recent advances in three-phase PFC models capable of simulating vapor-liquid-solid coexistence [19,20], as the vapor phase plays a crucial role in microstructure formation during processes such as chemical/physical vapor deposition, ice formation on surfaces through desublimation [21], and rapid solidification resulting in void-rich solidified material [22].

In what follows, we first adapt an existing vapor-liquid-solid PFC model that exhibits the usual density change upon solidification to describe anomalous density changes in materials such as water. The modified model could, in general, be applied to any pure material undergoing anomalous density change, and can be readily combined with other PFC literature techniques that allow for a variety of crystalline lattice structures [18,23], temperature and pressure dependence [19,24], and instantaneous elastic interactions [25]. The model is also amenable to further coarse-graining in space using a complex amplitude formulation [26,27], which we describe briefly. We apply the new PFC model and a preliminary complex amplitude formulation of said model to the solidification of a deeply quenched liquid droplet to demonstrate the effect of anomalous density change on the internal pressure and evolving microstructure of the droplet, comparing the results to recent experiments on cavitating water droplets [4].

II. MODEL

A. Vapor-liquid-solid PFC

A PFC model for a single material species is defined by a free energy functional $F[n]$ in terms of a spatially

varying density field $n(\mathbf{x})$. For simplicity, we here use a reduced (dimensionless) density field, which can be related to a real density by $n = (\rho - \bar{\rho})/\bar{\rho}$ where ρ is the dimensionful density and $\bar{\rho}$ is a reference density. The free energy is constructed to have local minima that correspond to the equilibrium phases of the physical system under consideration. Specifically, ordered phases, such as crystalline solids, are represented by a periodic oscillating density field, where the peaks of the oscillations are related to the time-averaged position of individual atoms, while disordered phases, such as fluids, have a constant density field.

For a vapor-liquid-solid coexistence system with regular density change on solidification (i.e., the solid phase exists at a higher density than the two fluid phases), previous work has used a free energy of the form [19,22]

$$F[n] = \int d\mathbf{x}\left(\sum_{l=2}^{4}\frac{1}{l}p_l n(\mathbf{x})^l + \sum_{l=2}^{4}\frac{1}{l}q_l n(\mathbf{x})n_{mf}(\mathbf{x})^{l-1}\right) - \frac{1}{2}\iint d\mathbf{x}_1 d\mathbf{x}_2 C^{(2)}(\mathbf{x}_1 - \mathbf{x}_2)n(\mathbf{x_1})n(\mathbf{x_2}), \quad (1)$$

where $n_{mf}(\mathbf{x})$ is the mean-field density obtained by applying a Gaussian smoothing operator to the microscopic density $n(\mathbf{x})$, the parameters p_l and q_l set the relative energies of the three accessible phases in thermodynamic equilibrium and are generally temperature dependent, and $C^{(2)}$ is a two-point correlation function that determines the lattice structure of the ordered solid phase. This functional form can be understood as inspired by classical density functional theory [17], where we approximate the full theory by truncating the correlation series up to the two-point correlation while keeping some information of the higher-order correlations through the choice of parameters p_l and q_l as well as through the nonlinear powers of mean-field density n_{mf}.

In this work, we will assume the simplest possible two-point correlation function, written in Fourier space as

$$\hat{C}^{(2)}(k) = B^x(2k^2 - k^4), \quad (2)$$

where k is the wave number and B^x is a possibly temperature-dependent parameter. This single-peak polynomial form of the correlation leads to a triangular lattice structure for the solid phase in two dimensions, or a bcc lattice in three dimensions. The width of the peak affects the surface energy of interfaces between thermodynamic bulk phases. More complex two-point correlation functions, as well as higher-order correlations, can be substituted into the model when other lattice structures or more fine-tuned control over interface energies is required [18,22,23].

The choice of parameters p_l, q_l, and B^x determines the model's phase diagram, which can be obtained by calculating the free energy density of all accessible thermodynamic phases. For the purpose of this calculation, we employ the so-called "one-mode approximation," which is the lowest-order periodic approximation for the density field of the solid phase [28]. In the case of a two-dimensional (2D) triangular lattice phase, this approximation is

$$n(\mathbf{x}) = n_o + A\left(\sum_{j=1}^{3} e^{i\mathbf{G}_j\cdot\mathbf{x}} + \text{c.c.}\right), \quad (3)$$

TABLE I. Chosen sets of parameters that lead to the vapor-liquid-solid PFC model exhibiting standard or anomalous density change upon solidification. Some of the parameters depend on the reduced temperature r.

	Standard density change	Anomalous density change
p_2	$r + 0.3$	$r + 0.3$
p_3	-0.5	-0.5
p_4	0.333	0.333
q_2	0	0
q_3	$35.0r - 12.01$	$51.8r - 11.8$
q_4	33.5	12.5
B^x	0.3	0.3
a_{20}	N/A	0.085
a_{21}	N/A	3.0
a_{22}	N/A	0.144
a_{23}	N/A	5.0

where n_o is the phase's average density, A is the amplitude of the oscillations, and $\mathbf{G}_j$ are the three lowest-order reciprocal lattice vectors. We also assume that, under this approximation, $n_{mf}(\mathbf{x}) = n_o$ since the mean-field density would not retain any lattice-scale information. Inserting this approximation into the free-energy functional in Eq. (1) and integrating over the lattice unit cell gives the mean-field free energy density

$$f(n_o, A) = \tfrac{1}{2}(p_2 + q_2)n_o^2 + \tfrac{1}{3}(p_3 + q_3)n_o^3 + \tfrac{1}{4}(p_4 + q_4)n_o^4 + 3(-B^x + p_2 + 2p_3 n_o + 3p_4 n_o^2)A^2 + 4(p_3 + 3p_4 n_o)A^3 + \tfrac{45}{2}p_4 A^4. \quad (4)$$

By minimizing Eq. (4) with respect to the amplitude A, we obtain the free-energy densities for the fluid phases (corresponding to setting $A = 0$) and for the solid phase ($A > 0$). After making the parameters dependent on a reduced (dimensionless) temperature r and repeating this calculation over a range of temperatures, a common tangent construction provides the phase diagram for the system. Figures 1(a) and 1(b) show typical free-energy densities for fixed r as a function of average density n_o when assuming a two-dimensional (2D) triangular lattice, using the temperature-dependent parameters given in the left column of Table I. These parameters yield the temperature-density phase diagram shown in Fig. 1(c), which displays a higher density for the solid phase than the liquid phase as is typical in most pure crystalline materials.

Note that PFC models can also access noncrystalline ordered phases, such as stripe phases in two dimensions and triangular rod phases in three dimensions. To obtain a physically valid phase diagram, the above one-mode approximation calculation must be repeated for each such phase [28] and parameters must be adjusted to ensure the undesired phases do not lie within the temperature-density ranges of interest.

B. Adding anomalous density change

To obtain a model with a phase diagram corresponding to a material that exhibits anomalous density change, it is necessary to "shift" the free-energy density minimum of the ordered solid phase to be between those of the two disordered

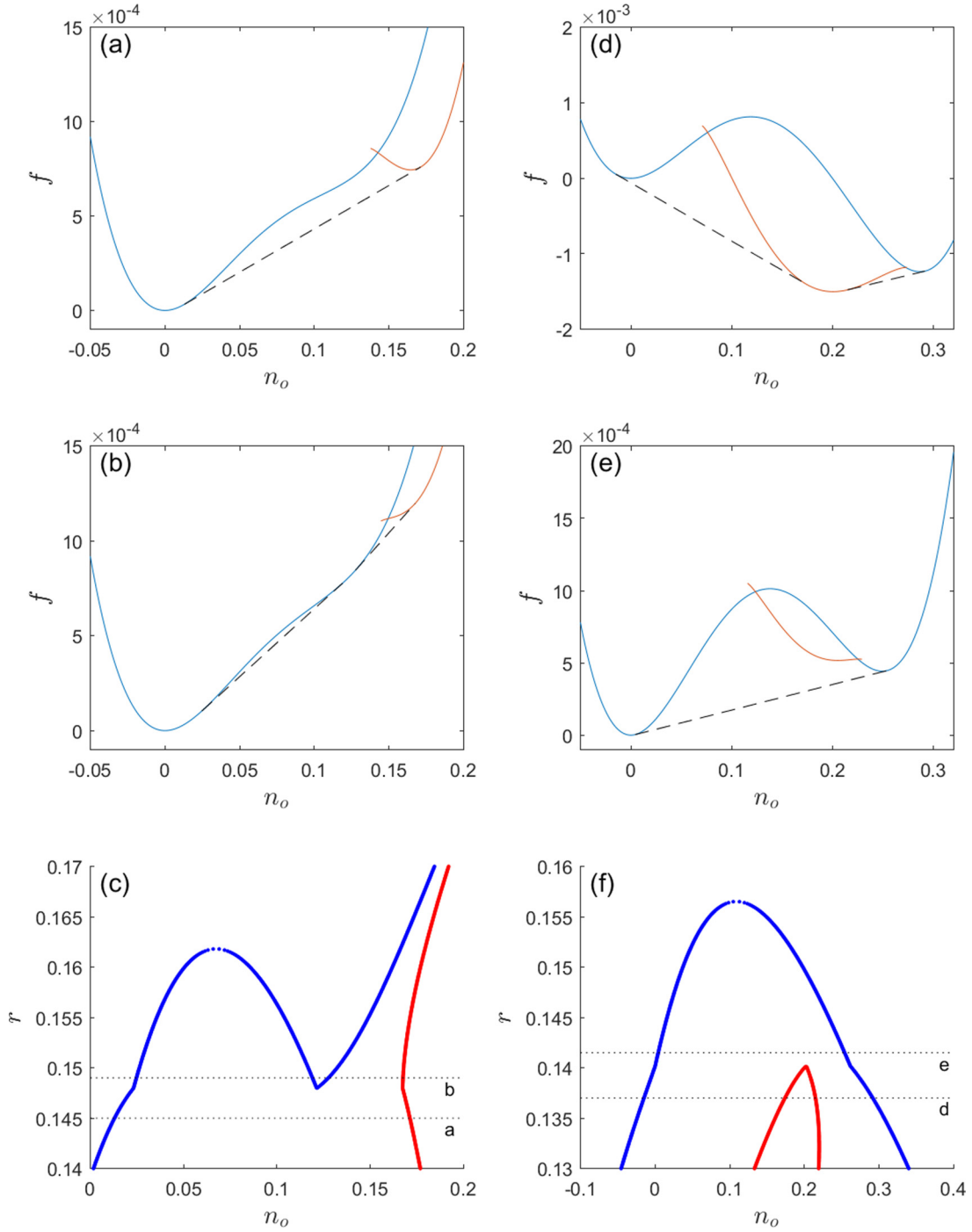

FIG. 1. Sample plots of mean-field free-energy densities $f(n_o)$ for the vapor-liquid-solid PFC model with standard and anomalous density change at solidification, along with the corresponding full phase diagrams. (a)–(c) correspond to a material with standard density change, while (d)–(f) for one with anomalous density change. The top two rows show the free-energy density of the fluid phase in blue and the solid in red, with the black dashed lines sketching the common tangents used to determine coexistence density ranges. These plots are calculated at temperatures (a) $r = 0.1450$, (b) $r = 0.1490$, (d) $r = 0.1370$, and (e) $r = 0.1415$. The bottom row of subfigures are the resulting temperature-density phase diagrams, where blue (red) denotes fluid (solid) coexistence density lines. The labeled dotted black lines show the temperatures at which the aforementioned free-energy density plots are calculated.

fluid phases. We do so here by adding an additional term $F_s[n]$ to the free-energy functional of Eq. (1). As such a term should only affect the energy of the solid phase, we assume it is proportional to a power of the one-mode approximation's amplitude A, ensuring the term vanishes in the fluid phases where $A = 0$ and its magnitude increases as the solid ordering emerges. We construct the simplest such term based on terms already present in Eq. (1),

$$F_s[n] = \int d\mathbf{x} \frac{a_2}{2} [n(\mathbf{x})^2 - n(\mathbf{x}) n_{mf}(\mathbf{x})], \tag{5}$$

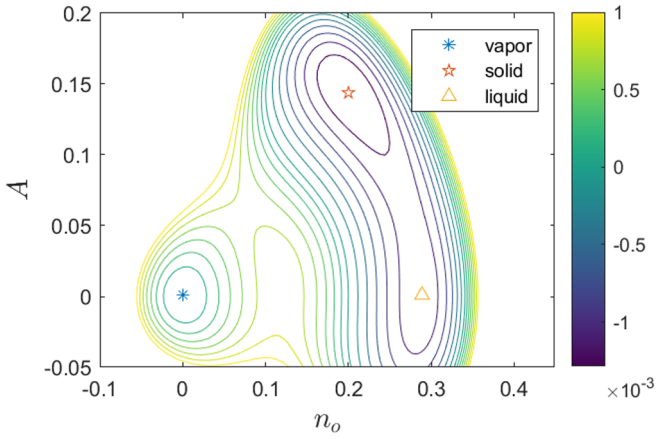

FIG. 2. Contour plot of the free-energy density $f(n_o, A)$ at temperature $r = 0.1370$, for the parameters in Table I corresponding to the anomalous density material. The location of the three phases' local minima are also shown. Note that minimizing this function with respect to A yields the free-energy density shown in Fig. 1(d).

where we have introduced a new parameter a_2 that controls the strength of this term. When the one-mode approximation is inserted into Eq. (5) and integrated as before, the free-energy density contribution of this new term is seen to be $3a_2A^2$. To control the solid phase's position on the phase diagram, we define a_2 to be dependent on both the reduced temperature r and the mean-field density $n_{mf}(\mathbf{x})$ according to

$$a_2 = a_{21}[n_{mf}(\mathbf{x}) - a_{20}]^2 + a_{23}(r - a_{22}), \tag{6}$$

where a_{2j} are constant subparameters. Figures 1(d) and 1(e) show some resulting free-energy densities using the parameters given in the right column of Table I, and Fig. 1(f) shows the corresponding phase diagram. The quadratic dependence of a_2 on $n_{mf}(\mathbf{x})$ helps constrain the solid phase's free-energy minimum along the density axis, enabling the desired shift of the solid phase's density, while the linear dependence on r ensures that the solid phase's region on the phase diagram does not extend past the fluid critical temperature. It is noted that expanding a_2 in Eq. (5) and comparing terms to those already present in Eq. (1) reveals that part of the added terms can also be accounted for by changing the values of q_2 and p_2. However, fully expanding Eq. (5) also reveals terms of the form $n^2 n_{mf}$ and $n^2 n_{mf}^2$, which do not correspond to existing terms in the original model of Eq. (1). The shape of the obtained phase diagram can be further tuned (e.g., to have a smaller density gap between liquid and solid, and a smaller pure-solid region), but doing so comes at the cost of increased numerical stiffness of the model; in what follows we will thus work with the parametrization shown in the right column of Table I, which leads to the phase diagram of Fig. 1(f).

One caveat in using solely the term $F_s[n]$ of the form given in Eq. (6) to shift the solid phase's energy minimum is a lack of control over the energy barriers between the three phases' minima in the resulting energy landscape. Figure 2 plots the contours of the free-energy density $f(n_o, A)$, including the effects of the shift term $F_s[n]$, before the minimization with respect to amplitude A is applied. We see that, for the chosen parameters, the minima corresponding to the solid and liquid phases occupy relatively shallow basins. This has implications for the dynamical (meta)stability of the respective phases as well as for the interfacial energies between bulks. While this limitation will not be an issue for the numerical experiment we present in Sec. III, further work is currently underway to allow finer control over the energy landscape, including through an investigation of the complex amplitude formulation of the model described in Sec. II D.

C. Dynamics

The free-energy function of Eq. (1) [including the added term of Eq. (5)] can be used to drive the dynamical evolution of the density field $n(\mathbf{x})$. As the next section of this work will examine a system in which rapid elastic effects dominate the dynamics, we assume two-time dynamics that relax elastic modes much faster than diffusion processes. This is done by adopting the damped PFC wave equation of motion developed by Stefanovich *et al.* [25],

$$\tau \frac{\partial^2 n}{\partial t^2} + \frac{\partial n}{\partial t} = \nabla^2 \frac{\delta F}{\delta n}, \tag{7}$$

where the parameter τ determines the wave propagation distance. For $\tau \to 0$ one recovers the more commonly used PFC equation of motion describing purely diffusive dynamics, while large τ approaches the limit of instantaneous elastic relaxation of the system (which comes at the cost of requiring increasingly small time steps for numerical simulations). Sufficiently large τ ensures that wavelike excitations propagate at length scales commensurate with the simulated system [25,29]. The value of τ does not affect the thermodynamics of coexisting phases predicted by the phase diagram calculation. The dynamics provided by Eq. (7) are known to be sufficient for reproducing elastic and plastic phenomena including, e.g., the reverse Hall-Petch effect [30] and complex defect evolution [31].

To validate our phase diagram, we use Eq. (7) with $\tau = 0$ to simulate systems consisting of 2D slabs of the various coexisting phases in the phase diagram of Fig. 1(f) at appropriate temperature and average density values. Periodic boundary conditions are used. Figure 3 shows the equilibrium density field $n(\mathbf{x})$ in each slab system, and the corresponding local average density field $n_{mf}(\mathbf{x})$ along the long axis, for different coexistence scenarios achievable with the model. We find that the dynamically obtained values for coexistence densities are within 5% difference from those predicted by the phase diagram based on the one-mode approximation, as is typical for such calculations applied to PFC models.

D. Complex amplitude formulation

The presented PFC model can be coarse-grained by reformulating the free-energy functional of Eq. (1) in terms of complex amplitude fields [26,27,32,33]. Such coarse-graining allows the simulation of larger systems, possibly bridging the gap between PFC models and more traditional PF models. Further, the reformulated free-energy functional allows finer control over its energy landscape, a focus of future work with the anomalous density PFC model that will require more flexibility in interfacial energies.

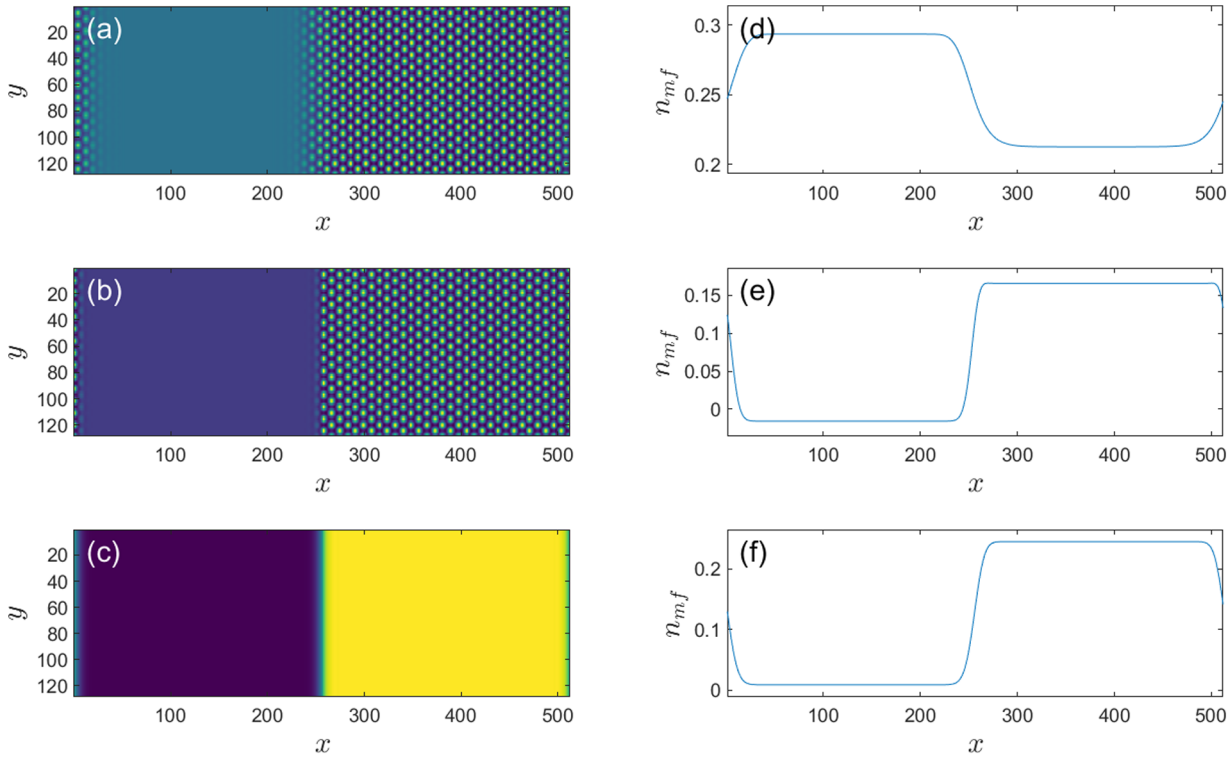

FIG. 3. Dynamical simulation of equilibrium phase coexistence for the system corresponding to the phase diagram in Fig. 1(f). (a)–(c) show the density field $n(\mathbf{x})$ for liquid-solid, vapor-solid, and vapor-liquid coexistence, respectively. Reduced temperatures used: (a),(b) $r = 0.1370$ (below triple point) and (c) $r = 0.1430$ (above triple point). (d)–(f) show the corresponding plots of $n_{mf}(\mathbf{x})$ along the x axis. Distances are in simulation grid units.

Here, we summarize the process for obtaining an amplitude formulation for our model. We expand the PFC density field in a manner similar to Eq. (3),

$$n(\mathbf{x}) = \bar{n}(\mathbf{x}) + \sum_{j=1}^{3} A_j(\mathbf{x}) e^{i\mathbf{G}_j\cdot\mathbf{x}} + \text{c.c.}, \tag{8}$$

where $\bar{n}(\mathbf{x})$ is the long-wavelength density and $A_j(\mathbf{x})$ are the complex amplitudes corresponding to each $\mathbf{G}_j$. Unlike in Eq. (3), $\bar{n}(\mathbf{x})$ and $A_j(\mathbf{x})$ are proper fields varying on length scales significantly larger than atomic spacings. Applying this expansion to Eq. (1) including the anomalous density term of Eq. (5) and following volume-averaging techniques [27], we obtain an amplitude model defined by a free-energy functional,

$$\begin{aligned} F_A[A_j,\bar{n}] = \int d\mathbf{x}\Bigg\{ & \sum_{l=2}^{4}\frac{1}{l}(p_l+q_l)\bar{n}^l + \Phi^2\left(\frac{1}{2}p_2 + p_3\bar{n} + \frac{3}{2}p_4\bar{n}^2 + \frac{1}{2}[a_{21}(\bar{n}-a_{20})^2 + a_{23}(r-a_{22})]\right) \\ & + \left(\prod_{j=1}^{3}A_j + \text{c.c.}\right)(2p_3 + 6p_4\bar{n}) + \frac{3}{4}p_4\left(\Phi^4 - 2\sum_{j=1}^{3}|A_j|^4\right) - \frac{1}{2}\bar{n}\mathcal{F}^{-1}[\hat{C}^{(2)}(|\mathbf{k}|)\hat{\bar{n}}(\mathbf{k})] \\ & - \frac{1}{2}\sum_{j=1}^{3}\left(A_j^*\mathcal{F}^{-1}\left[\hat{C}^{(2)}(|\mathbf{k}+\mathbf{G}_j|)\hat{A}_j(\mathbf{k})\right] + \text{c.c.}\right)\Bigg\}, \end{aligned} \tag{9}$$

where $\mathcal{F}^{-1}[\cdots]$ indicates the application of the inverse Fourier transform; $\hat{C}^{(2)}$, $\hat{\bar{n}}$, and $\hat{A}_j$ are the Fourier transforms of their respective function and fields; and we introduced the shorthand $\Phi^2 = 2\sum_{j=1}^{3}|A_j|^2$. We additionally apply a low-pass filter to the term $\mathcal{F}^{-1}[\hat{C}^{(2)}(|\mathbf{k}|)\hat{\bar{n}}(\mathbf{k})]$ to avoid periodic instabilities possibly emerging in the long-wavelength density field [27,33]. In this work, the evolution equations for the reformulated fields are obtained by assuming nonconserved damped wave dynamics for $A_j(\mathbf{x})$ and conserved damped wave dynamics for $\bar{n}(\mathbf{x})$, of the form

$$\tau\frac{\partial^2 A_j}{\partial t^2} + \frac{\partial A_j}{\partial t} = -\frac{\delta F_A}{\delta A_j^*}; \quad \tau\frac{\partial^2\bar{n}}{\partial t^2} + \frac{\partial\bar{n}}{\partial t} = \nabla^2\frac{\delta F_A}{\delta\bar{n}}. \tag{10}$$

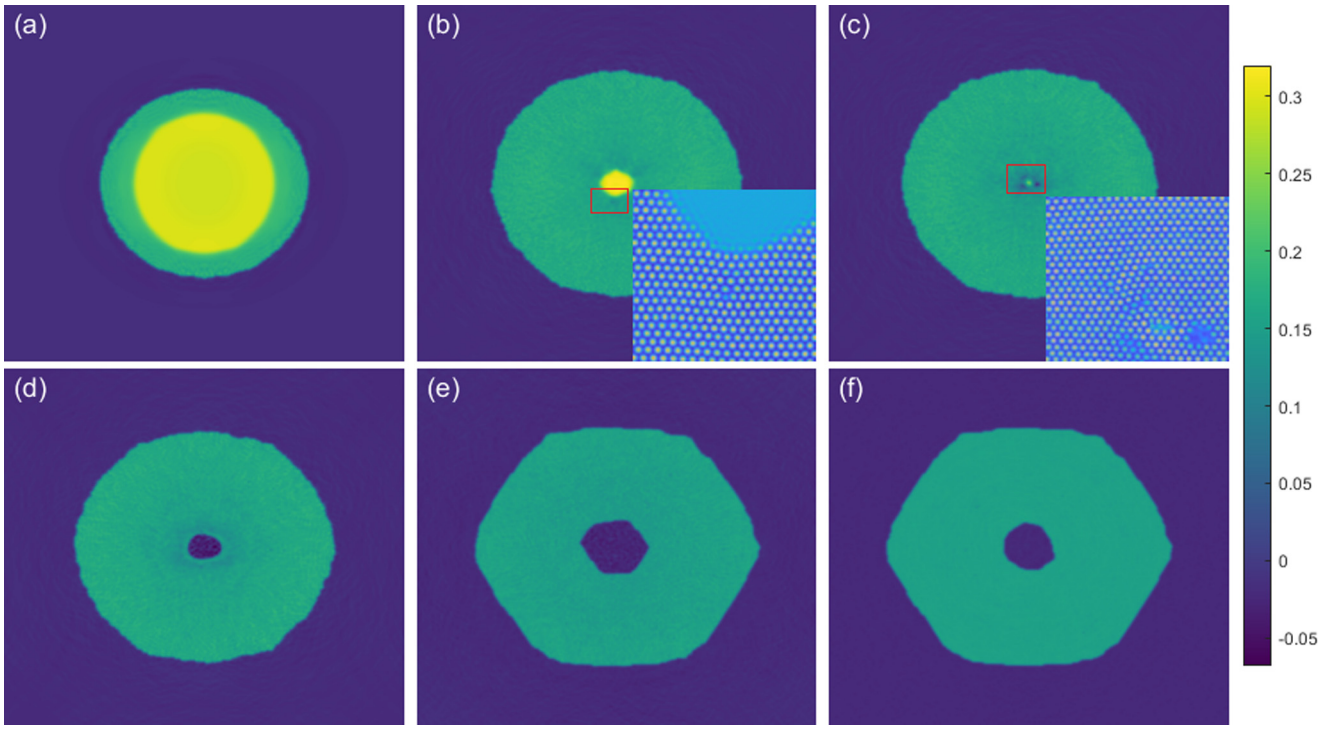

FIG. 4. Mean-field density $n_{mf}(\mathbf{x})$ of a solidifying icelike droplet at different snapshots of simulation time: (a) $t = 2\times10^5$, (b) $t = 9\times10^5$, (c) $t = 1\times10^6$, (d) $t = 1.1\times10^6$, (e) $t = 2\times10^6$, and (f) $t = 4\times10^6$. Insets in (b) and (c) show the zoomed-in density field $n(\mathbf{x})$ within the denoted red rectangles in the main images. The color bar corresponds to the average density axis of Fig. 1(f).

III. APPLICATION OF PFC MODEL TO FREEZING DROPLET

The anomalous density change PFC model described in Sec. II B is used to study defect formation and cavitation during rapid solidification in a deeply quenched liquid droplet, a process inspired by the recent experimental work of Wildeman *et al.* [4]. In the cited study, these authors examined supercooled water droplets freezing from the outside inward and building up a high internal pressure that eventually results in the frozen droplets developing vapor cavities and subsequently exploding. While it is presently numerically infeasible to use PFC modeling to simulate droplets at the millimeter length scales required for both cavitation and explosive effects, density effects leading to cavitation can be observed at much smaller system sizes attainable by PFC. Furthermore, although it is feasible to construct quantitative phase diagrams for a PFC model (see, for example, work on a quantitative aluminum phase diagram [22]) and include ice's hexagonal structure by an appropriate choice of correlation functions [23], we choose here to focus on the qualitative role of anomalous density change on the freezing process. As such, we use the model parameters and correlation function corresponding to the dimensionless phase diagram of Fig. 1(f) and consider a 2D triangular lattice to model the solid phase.

The dynamics of a solidifying droplet are simulated in two spatial dimensions via Eq. (7) using a semi-implicit spectral method. Our simulation system contains 2048×2048 grid points, with a dimensionless grid size of $\Delta x = 0.79$ for each mesh element. This grid size corresponds to approximately $1/9$ the lattice constant of our crystalline lattice. The numerical time step of our simulations is $\Delta t = 0.2$. Solidification is examined at a reduced model temperature of $r = 0.1370$. The initial state of our system is a near-circular liquid bulk seeded by a surrounding thin solid layer, with the rest of the system being vapor. The liquid and vapor densities are set to their coexistence values as per the phase diagram, while the solid density is set to its higher coexistence value (corresponding to coexistence with liquid). As rapid elastic relaxation is necessary to emulate the physical process observed by Wildeman *et al.* in their experiments, we set $\tau = 1\times10^6$. However, care must be taken to minimize initial transient behavior in the dynamics when using the second-order time dynamics inherent in Eq. (7). We thus gradually increase the parameter τ from 0 to 1×10^6 over a dimensionless simulation time ranging from $t = 0$ to 1400, which is a small enough fraction of the total simulation time to ensure that negligible solidification has yet taken place.

Figure 4 shows snapshots of the mean-field density $n_{mf}(\mathbf{x})$ of a solidifying drop of liquid simulated with our PFC model. We observe the initial thin solid shell expanding both inwards and outwards as the higher-density liquid solidifies and the excess density diffuses outwards. As the droplet nears complete solidification at simulation time $t \approx 1\times10^6$, defects form near the remaining liquid pool at the center. These nucleate vapor pockets coalesce into a cavity that subsequently "tears" into the center of the solidified droplet. The insets in Figs. 4(b) and 4(c) show the atomic-scale structure of the microscopic density field $n(\mathbf{x})$, which include topological

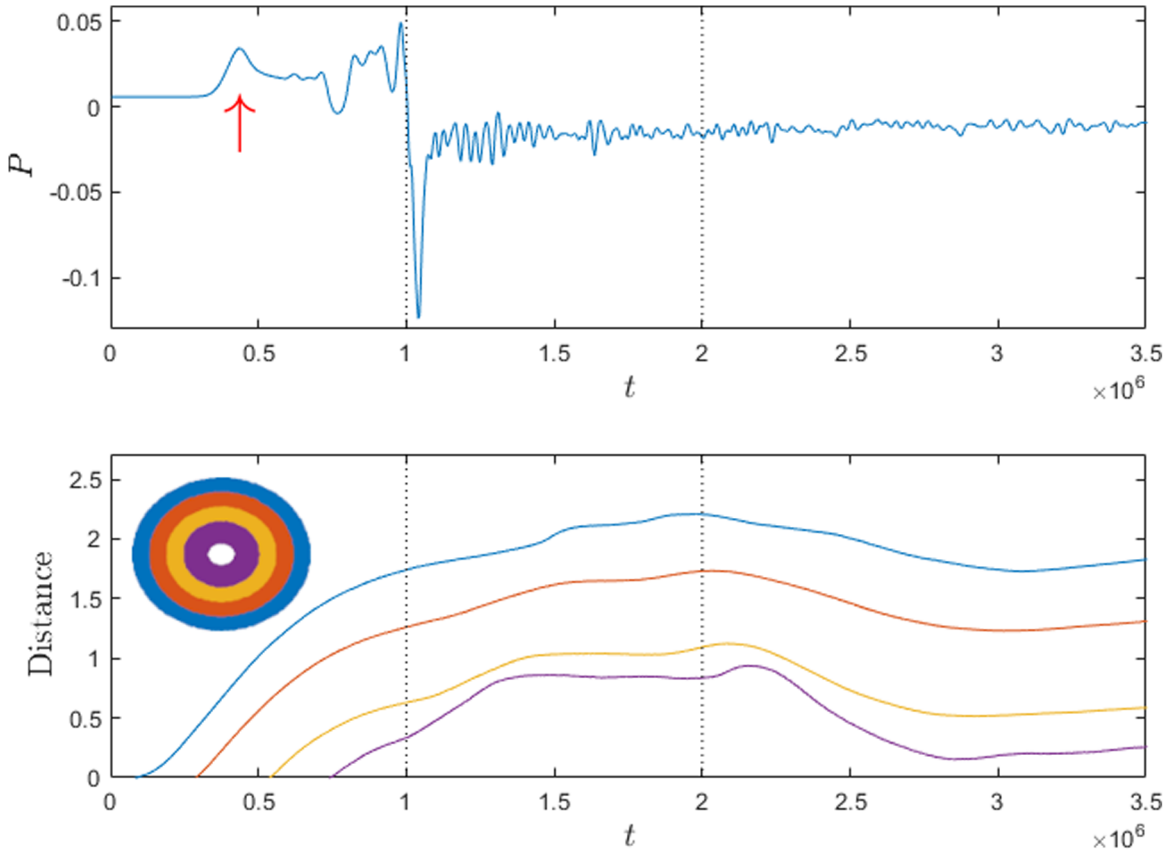

FIG. 5. Top: Plot of the estimated dimensionless pressure P at the center of the solidifying droplet as a function of dimensionless simulation time. The red arrow denotes a pressure fluctuation that is due to a transient shock wave, rather than due to the overdensification of the liquid (the latter of which occurs more gradually up to $t \approx 1\times10^6$). Bottom: Plot of the radially averaged outward displacement of atomic peaks of $n(\mathbf{x})$ at different radial shells of the solidifying droplet. Distances are in lattice constants. The top-left inset of the bottom frame shows a sketch of the droplet, with each shell colored as the corresponding displacement curve in the main plot. Top and bottom: the vertical dotted lines denote reference times corresponding to Fig. 4(c) (left line) where cavitation begins and Fig. 4(e) (right line) where the cavity approaches its maximum size.

defects and emerging nanocavities that appear towards the end of solidification and the start of the cavitation process. The nucleated cavity continues to expand for some time, reaching its maximum radius at time $t \approx 2\times10^6$ [Fig. 4(e)]. Eventually, the solidified droplet approaches its final equilibrium size, and the cavity begins to shrink (i.e., heal), ultimately fully recrystallizing.

To understand the source of the cavitation during solidification exemplified by Fig. 4, we track the effective pressure in our model following the approach of Refs. [19,20]. We compute the (dimensionless) functional generalization of the grand potential of the system,

$$\Omega = F[n] - \int d\mathbf{x}\left((n+1)\frac{\delta F}{\delta n}\right), \tag{11}$$

where $F[n]$ is the free-energy functional given by Eq. (1). We use the fact that thermodynamic pressure is given by $P = -\frac{\Omega}{V}$ over a volume V of a homogeneous phase to obtain an estimate for position-based pressure on length scales on the order of a few lattice constants. This estimated value of pressure reduces to the "true" thermodynamic pressure when at equilibrium and far from interfaces. The top plot of Fig. 5 shows the estimated pressure at the center of the freezing droplet, which is the last part of the droplet to solidify. The first peak of the pressure, indicated by a red arrow, was observed to be due to a transient shock wave that traveled from the solid-liquid interface at simulation start, and occurs at a point in time where the liquid is still far from fully vanishing. This shock-wave-induced peak would be more significant, to the point of drowning out the rest of the pressure signal, if we had not applied the previously described method to minimize initial transient behavior. Following this first peak, we observe the average pressure increases gradually (i.e., averaging over the occasional reflections of the initial shock wave) until $t \approx 1\times10^6$, corresponding to Fig. 4(c). The pressure then abruptly dips as cavitation begins at the center, and eventually rises back to a constant value as the pressure equilibrates throughout the system.

In their experiments, Wildeman *et al.* also observe vapor cavities appearing during rapid solidification of water droplets, and later healing in the freezing droplets [4]. Solidifying droplets are described in their work to behave as oscillators. Namely, the interior liquid overpressurizes

initially, due to the lower-density solid expanding inward and pushing into incompressible liquid in the center, which then leads to the solid shell being pushed outwards (i.e., overshooting the shell's equilibrium position set in at solidification), eventually causing the pressure in the center to drop low enough to cause cavitation. Whether the solid shell then proceeds to move back inwards or instead breaks free and explodes depends on the competition between the surface energy cost of forming a crack versus the elastic energy released by flying apart. The experimental droplets are estimated to require a radius greater than 50 μm in order to explode through this process. Based on the parameters of our PFC model, we expect our droplet, which has a radius on the order of 20 nm, would require highly unphysical surface energies to explode. In general, PFC models, including their derived amplitude formulations, are not yet capable of attaining the droplet sizes required to observe fully explosive behavior. Nevertheless, the observed cavitation in our simulated PFC droplet and the internal damped pressure oscillation it exhibits qualitatively agree with the behavior observed in the experimental droplets up to the time before they explode. Wildeman *et al.* also note that other experiments involving smaller physical droplets observe sharp drops in explosion probability with decreasing radius [34,35], which is also consistent with our simulated droplet's behavior.

We further explore the comparison between our PFC simulation and the experimental freezing droplets by tracking the movement of the atomic peaks of our density field $n(\mathbf{x})$. We divide the volume of the droplet into shells of equal radial thickness. Within each shell, we calculate the average radially outward displacement of all atomic peaks relative to their equilibrium position at solidification as a function of time. Atomic peaks solidifying beyond the initial droplet radius (due to density diffusion through the solid bulk) are not considered. The bottom plot of Fig. 5 shows the average displacement of each of the shells, measured in lattice constants. We observe that during solidification and for some time after the start of cavitation, the atomic peaks in all the shells are moving outwards on average. Eventually, the displacements plateau, and then reverse their direction soon after the cavity reaches its maximum size, the atomic peaks now moving inwards on average. At late times the displacements appear to slightly reverse their directions again. This expansion and contraction is likely the result of highly damped oscillation, analogous to that discussed in Ref. [4] in relation to the cavitation and cracking of freezing water droplets.

We remark that similar simulations conducted with $\tau = 0$ in Eq. (7) (i.e., diffusive dynamics alone) do not display any cavitation behavior, nor does atomic peak movement in such simulations indicate possibly oscillatory movement. This again indicates that such behavior is intrinsically tied to rapid elastic relaxation effects, rather than diffusive or thermodynamic effects, which is also consistent with the experimental hypothesis about the mechanism driving this process [4].

Finally, we briefly examine the behavior of the coarse-grained amplitude formulation of our PFC model, described in Sec. II D, when applied to the cavitating droplet system. A simulation system containing 512×512 grid points is used, with a dimensionless grid size of $\Delta x = 1.5$ for each mesh element and a numerical time step $\Delta t = 1.0$. A reduced model temperature of $r = 0.1370$ is used as before. The reduced size of the system compared to the previously described results allows the use of a smaller value for τ, thus we set $\tau = 1\times10^5$. Figure 6 shows snapshots of the long-wavelength density field $\bar{n}(\mathbf{x})$, displaying similar cavitation behavior as in the snapshots of Fig. 4. The solid-vapor interfaces display less faceting than in the previous PFC simulation, likely due to the coarse-graining process affecting the interface energy anisotropy.

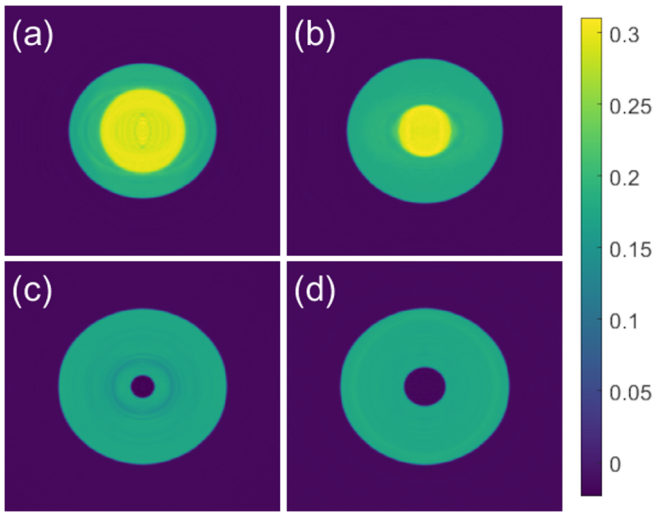

FIG. 6. The amplitude formulation's long-wavelength density field $\bar{n}(\mathbf{x})$ for a solidifying icelike droplet at different snapshots of simulation time: (a) $t = 5\times10^4$, (b) $t = 1\times10^5$, (c) $t = 2\times10^5$, and (d) $t = 3\times10^5$.

IV. CONCLUSION

We have introduced a PFC model for the solidification of materials exhibiting anomalous density change upon freezing. This was done by adapting a generic vapor-liquid-solid PFC model with a term that modifies the energy minimum of the ordered solid phase to lie at a lower density than the disordered liquid phase. The resulting temperature-density phase diagram is reminiscent of that of materials displaying anomalous density change on freezing, which include hexagonal ice and silicon. Using two-time relaxation-diffusion dynamics, we used the model to investigate and help elucidate the process of cavitation in supercooled water droplets observed in recent experiments.

Future work on this PFC model and its amplitude formulation will turn its attention towards better control of the free-energy density landscape, which would allow the study of systems with larger interfacial energies and higher relative stability between phases. An example of such systems includes frost spreading on hydrophobic surfaces [21,36], where ice spreads between supercooled droplets through competing mechanisms, including diffusive density flux through the vapor, ice bridges forming between droplets, and exploding droplet fragments nucleating new ice patches. Another path

of interest would be to examine larger scale microstructure formation in ice systems, including comparisons with known theoretical results on dendritic growth [37,38]. Finally, the amplitude formulation also opens the door to combining this work with the hydrodynamic PFC treatment of Heinonen *et al.* [39], which may better elucidate the oscillator behavior of freezing droplets.

ACKNOWLEDGMENTS

N.P. acknowledges the National Science and Engineering Research Council of Canada (NSERC) and the Canada Research Chairs (CRC) Program for financial support, and the McGill HPC Centre (Calcul Québec) for computing resources.

[1] J. Kruschwitz and J. Bluhm, Modeling of ice formation in porous solids with regard to the description of frost damage, Comput. Mater. Sci. **32**, 407 (2005).

[2] H. Cai and X. Liu, Freeze-thaw durability of concrete: Ice formation process in pores, Cem. Concr. Res. **28**, 1281 (1998).

[3] I. Vlahou and M. G. Worster, Ice growth in a spherical cavity of a porous medium, J. Glaciol. **56**, 271 (2010).

[4] S. Wildeman, S. Sterl, C. Sun, and D. Lohse, Fast Dynamics of Water Droplets Freezing from the Outside In, Phys. Rev. Lett. **118**, 084101 (2017).

[5] A. Lauber, A. Kiselev, T. Pander, P. Handmann, and T. Leisner, Secondary ice formation during freezing of levitated droplets, J. Atmos. Sci. **75**, 2815 (2018).

[6] S. Kim and M. M. Mench, Physical degradation of membrane electrode assemblies undergoing freeze/thaw cycling: Microstructure effects, J. Power Sources **174**, 206 (2007).

[7] T. Leimkuehler, R. Stephan, and S. Hansen, Development, testing, and failure mechanisms of a replicative ice phase change material heat exchanger, in *Proceedings of the 40th International Conference on Environmental Systems* (AIAA Press, Reston, VA, 2010), p. 6138.

[8] A. Gumennik, E. C. Levy, B. Grena, C. Hou, M. Rein, A. F. Abouraddy, J. D. Joannopoulos, and Y. Fink, Confined in-fiber solidification and structural control of silicon and silicon- germanium microparticles, Proc. Natl. Acad. Sci. USA **114**, 7240 (2017).

[9] K. Kutsukake, T. Abe, N. Usami, K. Fujiwara, I. Yonenaga, K. Morishita, and K. Nakajima, Generation mechanism of dislocations and their clusters in multicrystalline silicon during two-dimensional growth, J. Appl. Phys. **110**, 083530 (2011).

[10] M. G. Tsoutsouva, V. A. Oliveira, D. Camel, T. N. T. Thi, J. Baruchel, B. Marie, and T. A. Lafford, Segregation, precipitation and dislocation generation between seeds in directionally solidified mono-like silicon for photovoltaic applications, J. Cryst. Growth **401**, 397 (2014).

[11] M. Le Dantec, M. Abdulstaar, M. Leparoux, and P. Hoffmann, Epitaxial growth of silicon on silicon wafers by direct laser melting, Materials **13**, 4728 (2020).

[12] D. K. Fork, G. B. Anderson, J. B. Boyce, R. I. Johnson, and P. Mei, Capillary waves in pulsed excimer laser crystallized amorphous silicon, Appl. Phys. Lett. **68**, 2138 (1996).

[13] M. Matsumoto, S. Saito, and I. Ohmine, Molecular dynamics simulation of the ice nucleation and growth process leading to water freezing, Nature (London) **416**, 409 (2002).

[14] G. Moras, A. Klemenz, T. Reichenbach, A. Gola, H. Uetsuka, M. Moseler, and L. Pastewka, Shear melting of silicon and diamond and the disappearance of the polyamorphic transition under shear, Phys. Rev. Materials **2**, 083601 (2018).

[15] W. J. Boettinger, J. A. Warren, C. Beckermann, and A. Karma, Phase-field simulation of solidification, Annu. Rev. Mater. Res. **32**, 163 (2002).

[16] H. K. Lin and C. W. Lan, Three-dimensional phase field modeling of silicon thin-film growth during directional solidification: Facet formation and grain competition, J. Cryst. Growth **401**, 740 (2014).

[17] K. R. Elder, N. Provatas, J. Berry, P. Stefanovic, and M. Grant, Phase-field crystal modeling and classical density functional theory of freezing, Phys. Rev. B **75**, 064107 (2007).

[18] M. Greenwood, N. Provatas, and J. Rottler, Free Energy Functionals for Efficient Phase Field Crystal Modeling of Structural Phase Transformations, Phys. Rev. Lett. **105**, 045702 (2010).

[19] G. Kocher and N. Provatas, New Density Functional Approach for Solid-Liquid-Vapor Transitions in Pure Materials, Phys. Rev. Lett. **114**, 155501 (2015).

[20] Z.-L. Wang, Z. Liu, Z.-F. Huang, and W. Duan, Minimal phase-field crystal modeling of vapor-liquid-solid coexistence and transitions, Phys. Rev. Materials **4**, 103802 (2020).

[21] A. A. Yancheshme, G. Momen, and R. J. Aminabadi, Mechanisms of ice formation and propagation on superhydrophobic surfaces: A review, Adv. Colloid Interface Sci. **279**, 102155 (2020).

[22] P. Jreidini, T. Pinomaa, J. M. K. Wiezorek, J. T. McKeown, A. Laukkanen, and N. Provatas, Orientation Gradients in Rapidly Solidified Pure Aluminum Thin Films: Comparison of Experiments and Phase-Field Crystal Simulations, Phys. Rev. Lett. **127**, 205701 (2021).

[23] M. Seymour and N. Provatas, Structural phase field crystal approach for modeling graphene and other two-dimensional structures, Phys. Rev. B **93**, 035447 (2016).

[24] G. Kocher and N. Provatas, Thermodensity coupling in phase-field-crystal-type models for the study of rapid crystallization, Phys. Rev. Materials **3**, 053804 (2019).

[25] P. Stefanovic, M. Haataja, and N. Provatas, Phase-Field Crystals with Elastic Interactions, Phys. Rev. Lett. **96**, 225504 (2006).

[26] N. Goldenfeld, B. P. Athreya, and J. A. Dantzig, Renormalization group approach to multiscale simulation of polycrystalline materials using the phase field crystal model, Phys. Rev. E **72**, 020601(R) (2005).

[27] N. Ofori-Opoku, J. Stolle, Z.-F. Huang, and N. Provatas, Complex order parameter phase-field models derived from structural phase-field-crystal models, Phys. Rev. B **88**, 104106 (2013).

[28] N. Provatas and K. R. Elder, *Phase-Field Methods in Materials Science and Engineering* (Wiley, New York, 2011).

[29] S. Majaniemi, M. Nonomura, and M. Grant, First-principles and phenomenological theories of hydrodynamics of solids, Eur. Phys. J. B **66**, 329 (2008).

[30] P. Stefanovic, M. Haataja, and N. Provatas, Phase field crystal study of deformation and plasticity in nanocrystalline materials, Phys. Rev. E **80**, 046107 (2009).

[31] J. Berry, N. Provatas, J. Rottler, and C. W. Sinclair, Phase field crystal modeling as a unified atomistic approach to defect dynamics, Phys. Rev. B **89**, 214117 (2014).

[32] B. P. Athreya, N. Goldenfeld, and J. A. Dantzig, Renormalization-group theory for the phase-field crystal equation, Phys. Rev. E **74**, 011601 (2006).

[33] D.-H. Yeon, Z.-F. Huang, K. R. Elder, and K. Thornton, Density-amplitude formulation of the phase-field crystal model for two-phase coexistence in two and three dimensions, Philos. Mag. **90**, 237 (2010).

[34] P. V. Hobbs and A. J. Alkezweeny, The fragmentation of freezing water droplets in free fall, J. Atmos. Sci. **25**, 881 (1968).

[35] J. L. Brownscombe and N. S. C. Thorndike, Freezing and shattering of water droplets in free fall, Nature (London) **220**, 687 (1968).

[36] L. Hauer, W. S. Y. Wong, A. Sharifi-Aghili, L. Kondic, and D. Vollmer, Frost spreading and pattern formation on microstructured surfaces, Phys. Rev. E **104**, 044901 (2021).

[37] D. V. Alexandrov and P. K. Galenko, Thermo-solutal growth of an anisotropic dendrite with six-fold symmetry, J. Phys.: Condens. Matter **30**, 105702 (2018).

[38] L. V. Toropova, P. K. Galenko, D. V. Alexandrov, G. Demange, A. Kao, and M. Rettenmayr, Theoretical modeling of crystalline symmetry order with dendritic morphology, Eur. Phys. J.: Spec. Top. **229**, 275 (2020).

[39] V. Heinonen, C. V. Achim, J. M. Kosterlitz, S.-C. Ying, J. Lowengrub, and T. Ala-Nissila, Consistent Hydrodynamics for Phase Field Crystals, Phys. Rev. Lett. **116**, 024303 (2016).